Chinese Chemical Letters 36 (2025) 109738

Contents lists available at ScienceDirect

Chinese Chemical Letters

journal homepage: www.elsevier.com/locate/cclet

Graphene architecture interpenetrated with mesoporous carbon nanosheets promotes fast and stable potassium storage

Wenjing Xiong[a], Yulin Xu[a], Fangzhou Zhao[b], Baokai Xia[c], Hongqiang Wang[d], Wei Liu[a], Sheng Chen[c,*], Yongzhi Zhang[a,e,*]

[a] Institute of New Energy and Low-Carbon Technology (INELT), Sichuan University, Chengdu 610065, China
[b] College of Materials Science and Engineering, Sichuan University, Chengdu 610065, China
[c] School of Chemistry and Chemical Engineering, Nanjing University of Science and Technology, Nanjing 210094, China
[d] Guangxi Key Laboratory of Low Carbon Energy Material, Guangxi Normal University, Guilin 541004, China
[e] Yibin Industrial Technology Research Institute of Sichuan University, Yibin 644000, China

ARTICLE INFO

Article history:
Received 5 January 2024
Revised 3 February 2024
Accepted 6 March 2024
Available online 8 March 2024

Keywords:
Potassium storage
Graphene
Mesoporous carbon nanosheets
Composite
High-rate capability

ABSTRACT

Carbon materials are considered as prospective anode candidates for potassium ion batteries (PIBs). However, the low-rate capability is hampered by slow K^+ diffusion kinetics and obstructed electron transport of carbon-based anodes. In this work, calcium D-gluconate derived mesoporous carbon nanosheets (CGC) were interpenetrated into the architecture of reduced graphene oxides (RGO) to form the composites of two-dimensional (2D)/2D graphene/mesoporous carbon nanosheets (RGO@CGC). CGC as a rigid skeleton can prevent the graphene layers from restacking and maintain the structural stability of the 2D/2D carbon composites of RGO@CGC. The mesopores in CGC can shorten the path of ion diffusion and facilitate the penetration of electrolytes. RGO possesses the high surface-to-volume ratio and superior electron transport capability in the honeycomb-like 2D network consisting of sp^2-hybridized carbon atoms. Especially, the π-π stacking interaction between CGC and RGO enhances stable composite structure formation, expedites interlayer-electron transfer, and establishes three-dimensional (3D) ion transportation pathways. Owing to these unique structure, RGO@CGC exhibits fast and stable potassium storage capability. Furthermore, the effects of binders and electrolytes on the electrochemical performance of RGO@CGC were investigated. Finally, Prussian blue was synthesized as a positive electrode to explore the possibility of RGO@CGC as a full battery application.

Owing to the scarcity and imbalance distributions of lithium resources, there is a surge of exploration for alternative energy storage systems, particularly the potassium ion batteries (PIBs). Potassium resources are not only earth-abundant and cost-effective but also possess a low redox potential (−2.93 V *vs.* standard hydrogen electrode) [1–4]. Consequently, PIBs stand out as one of the most promising batteries. Nevertheless, one challenge problem is the large ion radius of K^+, prohibiting the efficient intercalation/deintercalation, leading to severe structure collapse of the electrode materials. Hence, it is imperative for PIBs to design an appropriate anode that can realize the stable insertion/extraction of K^+ [5,6].

At present, the anode materials for PIBs could be categorized as alloy compounds, transition metal compounds and carbon materials [7,8]. Carbon materials are present in the form of zero- (0D), one- (1D), two- (2D), and three-dimensions (3D). And the carbon quantum dot [9], carbon nanotubes [10], graphene [11], and porous carbon spheres [12] have been extensively investigated as anode for PIBs on account of their chemical stability, non-toxicity, low cost, safety, and outstanding conductivity. Notably, 2D carbon nanosheets represented by graphene with high surface-to-volume ratio as well as high electronic mobility, abundant charge-storage sites, ultrathin thickness, and large lateral size, have been broadly researched for PIBs [13,14]. However, graphene self-restacking occurs during repeated charging/discharging, reducing active sites, which is detrimental to energy storage [15]. Therefore, it is necessary to suppress the restacking of graphene sheets during charge and discharge process. In this respect, multidimensional and multiphase design would be an accessible approach to

* Corresponding authors.
E-mail addresses: sheng.chen@njust.edu.cn (S. Chen), zhangyz@scu.edu.cn (Y. Zhang).

https://doi.org/10.1016/j.cclet.2024.109738
1001-8417/

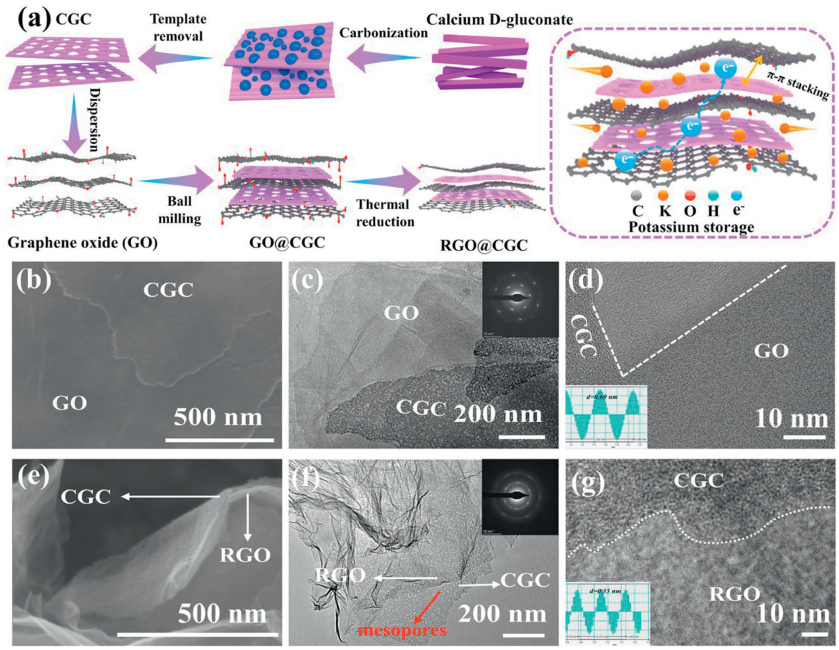

Fig. 1. Synthesis and morphology analysis. (a) Schematic of CGC and RGO@CGC preparation route. SEM images of (b) GO@CGC and (e) RGO@CGC. TEM, SAED and HRTEM images of (c, d) GO@CGC and (f, g) RGO@CGC.

obtain graphene composites with stable structure and outstanding performance [16,17].

The π-π stacking interaction is a non-covalent interaction between two aromatic ring and widely found between graphene and other compounds with π-electronic structures, which has received extensive investigation [18]. It has been reported that the existence of the π-π stacking interaction in carbon composites can significantly enhance electron transport and enable stable structure [19,20]. Despite of numerous graphene-based hybrids (such as porous carbon [21] and carbon nanofibers [22]) have been reported, the π-π stacking interactions between each component need to be strengthened to inhibit the restacking of the graphene and obtain sufficient space between the graphene sheets, achieving a robust structure and exceptional electron transport.

In this work, calcium D-gluconate derived mesoporous carbon nanosheets (CGC) are firstly prepared and then interpenetrated into the architecture of reduced graphene oxides (RGO) to form the composites of 2D/2D graphene/mesoporous carbon nanosheets (RGO@CGC). RGO@CGC demonstrates a high reversible capacity of 419.2 mAh/g at 0.1 A/g, superior rate performance (207.8 mAh/g at 2 A/g) and outstanding cyclic stability (204.2 mAh/g at 1 A/g after 1000 cycles). Additionally, the impacts of electrolytes and binders for the potassium storage are investigated, finding that potassium bis(fluoromethanesulfonyl)imide (KFSI) electrolyte and sodium carboxymethyl cellulose (CMC) binder could improve the initial coulombic efficiency (ICE) of RGO@CGC electrode. Finally, a full cell is assembled with RGO@CGC as the anode and Prussian blue (PB) as the cathode to demonstrate the feasibility of RGO@CGC for PIBs.

Calcium D-gluconate derived CGC is achieved through a self-template method, involving calcination of calcium D-gluconate followed by washing with hydrochloric acid. A homogeneous mixture of CGC and graphene oxide (GO) is prepared *via* ball milling, named GO@CGC. The product of the thermal reduction of GO@CGC is termed as RGO@CGC (Fig. 1a). As a comparison, RGO is acquired through the thermal reduction of GO. The micromorphology of GO, RGO and CGC is studied (Fig. S1 in Supporting information). GO consists of stacked platelets with ample wrinkles. RGO presents a corrugated morphology. CGC exhibits a lamellar with abundant mesopores. The high-resolution transmission electron microscope (HRTEM) pictures of RGO and CGC are displayed in Fig. S2 (Supporting information), manifesting that RGO has a multi-layer graphene stack structure with short-range graphite domain, as well as CGC has a mesoporous structure and disordered nature.

The scanning electron microscopy (SEM) and transmission electron microscopy (TEM) images of GO@CGC and RGO@CGC are depicted in Figs. 1b-g. It is evident that smooth CGC flakes, serving as a structural skeleton, are embedded within GO and remain tightly integrated post blending (Figs. 1b and c). After sintering, the rigid porous CGC flakes is interpenetrated with RGO layers and the 2D/2D carbon composite is formed (Figs. 1e and f). The HRTEM image of GO@CGC exhibits an ordered-disordered composite structure, and the measured average interlayer spacing is approximately 0.60 nm (Fig. 1d). The selected area electron diffraction pattern (SAED) reveals the presence of a hexagonally arranged lattice of carbon atoms that corresponds to GO (inset of Fig. 1c) [23]. HRTEM image of RGO@CGC is displayed in Fig. 1g, where RGO is stacked with CGC, and the mean layer spacing is approximately 0.35 nm. The corresponding SAED (inset of Fig. 1f) displays diffused ring around the center light spot, manifesting the coexistence disordered and overlapped crystalline structure [24]. CGC with lots of mesopores as a rigid skeleton would prevent the graphene layers from restacking, provide abundant mesoporous between carbon layers, and maintain structural stability of RGO@CGC composites. The rich mesopores would offer ample active sites, efficient transport path for K^+ and electrolyte penetration [25,26].

To investigate the phase composition and structure differences, X-ray diffraction (XRD) analysis is performed. As shown in Fig. 2a, RGO, CGC, and RGO@CGC all exhibit amorphous characteristics. Furthermore, the (002) peak for RGO@CGC appears at 25.05°, signifying a slight shift towards a smaller angle relative to the characteristic peak position of RGO (25.8°). This can be attributed to the inhibiting effect of CGC on the restacking of RGO sheets. Based on the Bragg's law, the calculated layer spacing for RGO@CGC and RGO is 0.355 nm and 0.345 nm, respectively. These values are significantly wider than graphite (0.336 nm). The enlarged layer spacing facilitates the intercalation/deintercalation of K^+ [27,28].

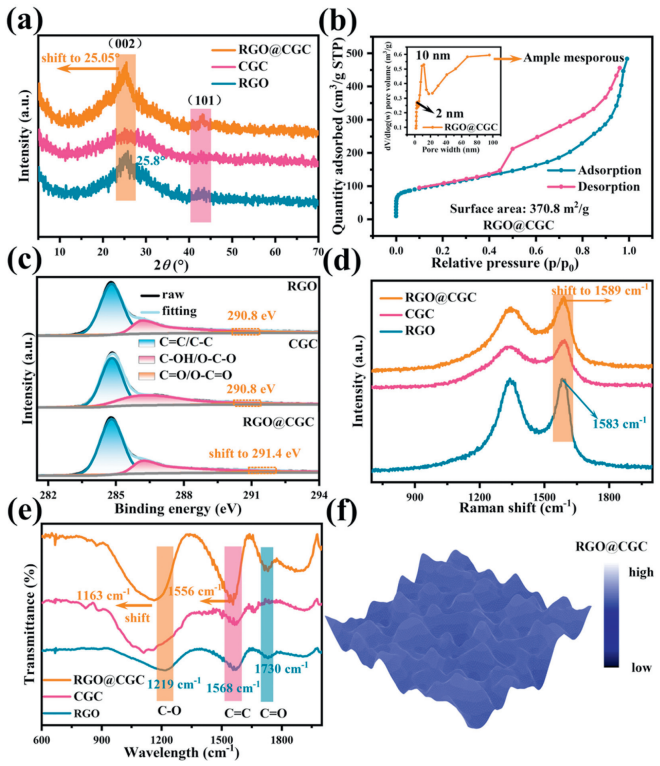

Fig. 2. Structure characterization of CGC, RGO, and RGO@CGC. (a) Wide angle XRD images. (b) N_2 adsorption/desorption isotherms and pore size distribution of RGO@CGC. (c) High-resolution of C 1s spectra. (d) *Ex-situ* Raman spectra. (e) FTIR spectra. (f) Laser confocal Raman mapping of RGO@CGC.

Furthermore, the nitrogen adsorption/desorption curves and pore size distribution plots are depicted in Fig. 2b and Fig. S3 (Supporting information). The specific surface areas of RGO, CGC and RGO@CGC are 258.1, 677.5, and 370.8 m^2/g, respectively, as calculated by the Brunauer-Emmett-Teller (BET) method. The larger specific surface area of RGO@CGC compared to RGO can be attributed to the intercalation of CGC, which provides ample mesoporous and effectively prevents graphene layers from restacking. The pore size peaks of RGO@CGC are located at 2 nm and 10 nm, indicating that RGO@CGC has ample pore structure. The coexistence of carbon and oxygen is revealed by the full spectrum of X-ray photoelectron spectroscopy (XPS) (Fig. S4 in Supporting information). The high-resolution C 1s spectra are presented in Fig. 2c. The peak position of C=O/O-C=O shifts in RGO@CGC owing to the electronic effect originating from the π-π stacking interaction between RGO and CGC within RGO@CGC [29]. Furthermore, the G-band of RGO@CGC is slightly shifted compared to RGO and CGC in Raman spectra (Fig. 2d). The Fourier transform infrared spectroscopy (FTIR) image shows that the C=C and C-O vibrations peaks of RGO@CGC exhibits shifts in relative to RGO (Fig. 2e). These results suggest the presence of conjugated π-π stacking between RGO and CGC [29–31]. Resistivity test results (Fig. S5 in Supporting information) manifest that RGO@CGC delivers superior conductivity which can be attributed to the π-π stacking interactions between RGO and CGC. Laser confocal Raman mapping spectrum is employed to evaluate the homogeneity of material mixing (Fig. 2f). These consistent waves indicate that RGO and CGC are uniformly distributed in RGO@CGC.

The electrochemical performances of RGO, CGC, and RGO@CGC are depicted in Fig. 3. The cyclic voltammetry (CV) curves of RGO@CGC are illustrated in Fig. 3a. A wide-range reduction peak is noticeable at ~0.55 V (*vs.* K^+/K) during the process of initial discharge, corresponding to solid electrolyte interface (SEI) formation [32,33]. The second and third CV curves overlap well, indicating good reversibility. The CV plots of RGO and CGC are featured in Figs. S6a and b (Supporting information). The CV curves of RGO display a poor overlap, indicating poor reversibility. The CV curves in second and third cycles of CGC replicate nicely, implying a satisfactory reversibility. Fig. 3b presents the galvanostatic charge/discharge (GCD) curves of RGO@CGC, within the voltage range of 0.01–3 V (*vs.* K^+/K). Its initial charge specific capacity reaches 419.7 mAh/g. The initial charge specific capacities of RGO and CGC are 390.4 and 270.5 mAh/g, respectively (Figs. S6c and d in Supporting information). The high reversible specific capacity of RGO@CGC can be attributed to wider layer spacing and ample mesoporous structure. The cyclic stability of RGO, CGC, and RGO@CGC at 0.1 A/g are depicted in Fig. 3c. After 100 cycles, RGO@CGC preserves a reversible specific capacity of 297.4 mAh/g, considerably higher than RGO (214.5 mAh/g) and CGC (240.9 mAh/g). The rate capability and long-term cyclic performance are elucidated in Fig. 3d. The initial charge specific capacity of RGO@CGC is 410.5 mAh/g at 0.1 A/g, and when the current density increases to 0.2, 0.5, 1, 2, 5, 10 A/g, the capacities are 323.9, 273.1, 259.0, 207.8, 161.1, 119.5 mAh/g, respectively, and the specific capacity regains to 227.3 mAh/g when the current density returns to 1 A/g. After 1000 cycles, RGO@CGC maintains a high specific capacity of 204.2 mAh/g, while RGO exhibits nearly negligible capacity, and CGC displays only 133.4 mAh/g. Fig. 3e exhibits the comparison of rate performance and long-term cyclic performance with previously reported carbonaceous materials for PIBs [34–43]. The favorable rate performance can be attributed to several factors: (1) The larger layer spacing facilitating K^+ embedding/deembedding; (2) The 2D/2D structure encouraging electron transport and interfacial reactions; (3) The mesoporous structure provided by CGC offering more active sites and accelerating electrolyte infiltration; (4) The π-π stacking effect promoting interlayer electron transport and constructing a 3D ion transport channel. The penetration of CGC inhibits the restacking of RGO, and π-π stacking interaction promotes the stable composite structure formation. These forms the foundation for the exceptional stability of RGO@CGC [19,44,45].

The structural transformations of RGO and RGO@CGC during potassium storage are investigated by *in-situ* XRD. With the increasing depth of discharge, the intensity of the (002) peak of RGO decreases and transitions to a smaller angle (Fig. 3f). This phenomenon aligns with previous literature, and is believed to stem from the disorderly transformation of the carbon microstructure coupled with the embedding of potassium ions [46,47]. During the charge process, the (002) peak could not return to original position and exhibits a shift towards a higher angle, indicating a decrease in the layer spacing of RGO and disruption of its interlayer structure. However, no significant variation is noted in the intensity and position of the (002) peak of RGO@CGC during the charge and discharge process (Fig. 3g), indicating excellent structural stability of RGO@CGC, which is consistent with its exceptional cyclic performance. Diffraction peaks around 16°, 17°, 18° and 24.5° can be attributed to the *in-situ* testing device of beryllium window. The XRD patterns of RGO@CGC tested in beryllium window and individual beryllium window are shown in Fig. S7 (Supporting information). Furthermore, the morphology of the RGO@CGC electrodes before cycling and after long-term cycling for 1000 cycles at 1 A/g are exhibited in Fig. S8 (Supporting information). The results indicate that the 2D/2D composite structure of RGO@CGC is maintained even after long-term cycling, demonstrating that the penetration of CGC can effectively inhibit the restacking of RGO and guarantee the structural stability.

To investigate the reason for superior rate capability of RGO@CGC, CV tests with various sweep rates and Galvanostatic Intermittent Titration Technique (GITT) measurement are conducted.

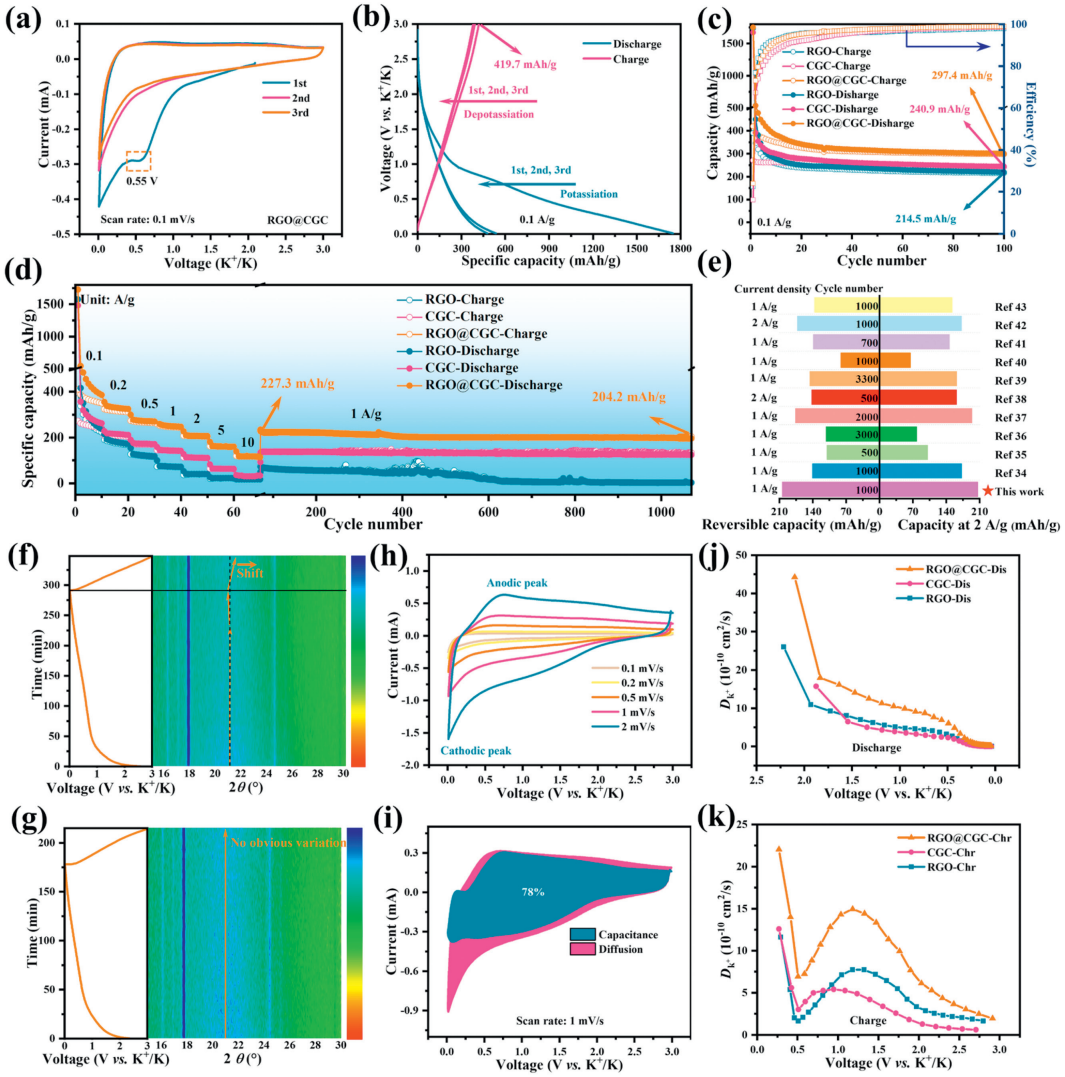

Fig. 3. Electrochemical measurements. (a) CV curves for RGO@CGC at 0.1 mV/s. (b) GCD curves for RGO@CGC. (c) Cyclic stability for RGO, CGC and RGO@CGC. (d) Rate performance from 0.1 A/g to 10 A/g and long-term cyclic performance at 1 A/g. (e) Comparison of rate performance and long-term cyclic performance with previously reported carbon-based anode materials for PIBs. The *in-situ* XRD image of (f) RGO and (g) RGO@CGC electrodes during the initial discharge–charge process. (h) CV curves of RGO@CGC with different sweep rates. (i) Capacitive contribution in RGO@CGC with the scan rate of 1 mV/s. (j, k) D_{K^+} are obtained from the GITT profiles during charge/discharge.

Based on CV curves with different sweep rates (Fig. 3h), the *b* value for reduction and oxidation peaks are 0.96 and 0.93 (Fig. S9 in Supporting information), respectively, providing evidence that the potassium storage process is controlled by capacitance and diffusion mechanisms. RGO@CGC delivers a ratio of capacitance contribution of 78% at 1 mV/s (Fig. 3i). Additionally, the contribution percentages of capacitive and diffusion control for different sweep speeds can be also observed from Fig. S10 (Supporting information). A notable trend emerges where the percentage contribution from capacitance progressively escalates with increasing sweep speed. Fig. S11 (Supporting information) shows the potential response of RGO, CGC, and RGO@CGC electrodes through GITT during charge/discharge after 3 activation cycles. The diffusion coefficient of K^+ (D_{K^+}) in RGO@CGC is higher than that of RGO and CGC at various voltages, calculated by GITT (Figs. 3j and k). The calculation method of D_{K^+} is provided in supplementary information [48,49]. The superior rate performance of RGO@CGC is attributed to a capacitance-dominated energy storage mechanism and a large D_{K^+}.

The ICE of RGO@CGC is only 24% in 0.8 mol/L KPF_6 in EC/DEC (hereinafter referred to as 0.8-M KFP_6) with polyvinylidene fluoride (PVDF) as binder, suggesting further advancements are required. Two strategies are employed to enhance the ICE. Firstly, it is investigated that the effect of electrolytes for RGO@CGC. 3 mol/L KFSI in DME (hereinafter referred to as 3-M KFSI) is introduced as an electrolyte to improve the ICE. Fig. S12 (Supporting information) exhibits the CV curve of RGO@CGC in 3-M KFSI electrolyte. The first charge capacity of RGO@CGC attains 520.3 mAh/g at 0.1 A/g, and the ICE increases to 33.3%, demonstrating a notable enhancement in contrast to 0.8-M KFP_6 as electrolyte (Fig. 4a). TEM images of SEI after the first cycle in both electrolytes are displayed in Figs. 4b and c. The SEI is smoother and has a thickness of approximately 13.21 nm in 3-M KFSI. However, the SEI in 0.8-M KFP_6 measures 25.19 nm. The SEI images after five cycles are displayed in Fig. S13 (Supporting information). After cycling for 5 cycles, the thickness of SEI in both electrolytes increases slightly. These results disclose that the decomposition of the 0.8-M KPF_6 electrolyte is more severe than that of the 3-M KFSI electrolyte in PIBs [50]. Furthermore, electrochemical impedance spectroscopy (EIS) is performed on both electrolytes (Fig. S14 in Supporting information). The resistance values are exhibited in Table S1 (Supporting information). Prior to cycling, the half-cell displays a larger ohmic resistance (R_S)

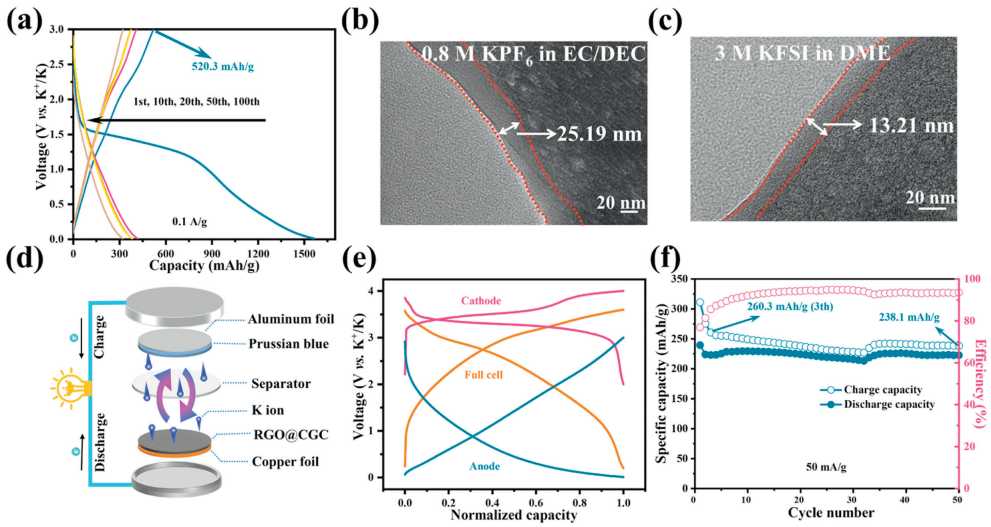

Fig. 4. Electrolyte optimization and full cell. (a) GCD profiles of RGO@CGC in 3-M KFSI. TEM images of SEI after the first cycle in (b) 0.8-M KFP_6 and (c) 3-M KFSI. (d) Schematic illustrating the configuration of the assembled coin-type PB||RGO@CGC cell. (e) GCD profiles of cathode, anode, and full cell. (f) Cyclic stability of full cell.

in 0.8-M KFP_6 as compared to 3-M KFSI. After the first cycle, the cell exhibits a small charge-transfer (R_{ct}) resistance and SEI resistance (R_{SEI}) in 3-M KFSI. SEI components are analyzed using XPS in two different electrolytes. Organic components overwhelmingly dominate the composition of SEI in 0.8-M KFP_6. In comparison, SEI in 3-M KFSI electrolyte contains more inorganic components (Fig. S15 in Supporting information). The SEI layer rich in inorganic content can promote the sustainability of the interphase and thus improve electrochemical performance [51]. Overall, less side reactions along with thin and effective SEI are the reasons for a higher ICE in 3-M KFSI.

In addition, CMC is substituted for PVDF as a binder. The GCD curves of RGO@CGC with CMC as binder in two electrolytes are shown in Fig. S16 (Supporting information). The ICE increased to 32% and 54% in 0.8-M KPF_6 and 3-M KFSI, respectively. The reason for this outcome is that PVDF-based electrode induces more side reactions and a thicker SEI in comparison to CMC-based electrode [52,53]. The SEM images of the RGO@CGC electrode before cycling and after initial cycle are shown in Fig. S17 (Supporting information). It shows that PVDF as the binder results in more side reactions on the surface of the electrodes, forming a thicker SEI.

Finally, we synthesize PB as the cathode and RGO@CGC as the anode. A full cell is assembled, and its cycle performance is assessed, as depicted in Fig. 4d. Here, considering the risk that solvent decomposition and KFSI could corrode the current collector at high voltage using 3-M KFSI [54–56], we still chose 0.8-M KPF_6 as electrolyte in full cell. PB is synthesized based on the literature [57]. The structure and cycle stability of PB are exhibited in Fig. S18. The charge and discharge profiles of the positive, negative, and full battery are exhibited in Fig. 4e. The charge specific capacity after three cycles stabilizes at 260.3 mAh/g (based on negative weight), and the capacity retention after 50 cycles is 91.5% relative to the third cycle (Fig. 4f), suggesting the potential for practical application.

In summary, benefiting from the unique 2D/2D graphene/mesoporous carbon nanosheet structure, RGO@CGC exhibits excellent rate performance and cyclic stability. Additionally, it is discovered that using 3-M KFSI as the electrolyte enhances the reversible capacity and ICE. Moreover, CMC as binder also can provide higher ICE compared to PVDF. Finally, a full cell is also assembled to certify practical application of RGO@CGC anode. This study not only designs structurally optimized electrode materials but also provides new insights into the mechanisms by which electrolytes influence electrochemical performance. Our research outlines a straightforward technique for manufacturing anode materials for PIBs, which could open doors for potential applications of PIBs in the future.

Declaration of competing interest

The authors declare that they have no known competing financial interests or personal relationships that could have appeared to influence the work reported in this paper.

Acknowledgments

The authors would like to acknowledge the financial support from the National Natural Science Foundation of China (No. 92163124), Foundation for the Sichuan University and Zigong City Joint research project (No. 2021CDZG-2), Foundation for the Sichuan University and Yibin City Strategic Cooperation Project (No. 2020CDYB-32) and Guangxi Key Laboratory of Low Carbon Energy Material (No. 2020GKLLCEM02). We appreciate Li Wu for assisting with Raman testing at Analytical & Testing Center Sichuan University and the New Energy and Low-Carbon Technology (INELT) of Sichuan University for SEM measurements.

Supplementary materials

Supplementary material associated with this article can be found, in the online version, at doi:10.1016/j.cclet.2024.109738.

References

[1] H. Zhang, W. Li, J. Pan, et al., J. Energy Chem. 73 (2022) 533–541.
[2] C. Shi, J. Xu, T. Tao, et al., Small Methods 8 (2024) 2301277.
[3] S. Wu, H. Peng, J. Xu, et al., Carbon 218 (2024) 118756.
[4] L. Li, D. Cheng, G. Zou, et al., J. Alloys Compd. 958 (2023) 170481.
[5] J. Sun, R. Tian, Y. Man, Y. Fei, X. Zhou, Chin. Chem. Lett. 34 (2023) 108233.
[6] G. Liu, Z. Sun, X. Shi, et al., Adv. Mater. 35 (2023) 2305551.
[7] H. Bi, X. He, L. Yang, et al., J. Energy Chem. 66 (2022) 195–204.
[8] M. Zhang, Y. Liang, F. Liu, et al., J. Mater. Chem. A 11 (2023) 8162–8172.
[9] L. Li, Y. Li, Y. Ye, et al., ACS Nano 15 (2021) 6872–6885.
[10] Y. Liu, Q. Deng, Y. Li, et al., ACS Nano 15 (2021) 1121–1132.
[11] Y.C. Chen, L. Qin, Y. Lei, et al., ACS Appl. Mater. Interfaces 11 (2019) 45578–45585.
[12] S. Dou, Q. Tian, T. Liu, et al., Small Sci. 2 (2022) 2200045.
[13] J. Han, C. Zhang, D. Kong, et al., Nano Energy 72 (2020) 104729.
[14] H.Y. Xu, H. Chen, C. Gao, ACS Mater. Lett. 3 (2021) 1221–1237.
[15] R. Raccichini, A. Varzi, S. Passerini, B. Scrosati, Nat. Mater. 14 (2015) 271–279.

[16] M. Hu, J. Song, H. Fan, et al., Chem. Eng. J. 451 (2023) 138452.
[17] Z. Jian, S. Hwang, Z. Li, et al., Adv. Funct. Mater. 27 (2017) 1700324.
[18] V. Georgakilas, J.N. Tiwari, K.C. Kemp, et al., Chem. Rev. 116 (2016) 5464–5519.
[19] P. Huang, T.Z. Xiong, S.H. Zhou, et al., ACS Appl. Mater. Interfaces 13 (2021) 16516–16527.
[20] Y. Wang, F.B. Meng, F. Huang, et al., ACS Appl. Mater. Interfaces 12 (2020) 47811–47819.
[21] J. Wei, Y. Hu, Y. Liang, et al., Adv. Funct. Mater. 25 (2015) 5768–5777.
[22] M.K. Liu, P. Zhang, Z.H. Qu, et al., Nat. Commun. 10 (2019) 3917.
[23] P. Kumar, G.Andersson Harish, et al., Ceram. Int. 47 (2021) 14862–14878.
[24] L.L. Liu, M.Z. An, P.X. Yang, J.Q. Zhang, Int. J. Electrochem. Sci. 10 (2015) 1582–1594.
[25] Y. Yan, Y.X. Yin, Y.G. Guo, L.J. Wan, Adv. Energy Mater. 4 (2014) 1301584.
[26] X. Pan, B. Xi, H. Lu, et al., Nano-Micro Lett. 14 (2022) 163.
[27] J.M. Chen, Y. Cheng, Q.B. Zhang, et al., Adv. Funct. Mater. 31 (2021) 2007158.
[28] Z. Sun, Y. Chen, B. Xi, et al., Energy Storage Mater. 53 (2022) 482–491.
[29] H. Wang, P.F. Hu, J. Yang, et al., Adv. Mater. 27 (2015) 2348–2354.
[30] S. Wang, X. Sun, F. Xu, et al., Carbon 179 (2021) 469–476.
[31] B.A. Aragaw, J. Nanostruct. Chem. 10 (2019) 9–18.
[32] X. Lu, J. Zhou, L. Huang, et al., Adv. Energy Mater. 14 (2024) 2303081.
[33] J. Gong, G. Zhao, J. Feng, et al., ACS Nano 14 (2020) 14057–14069.
[34] D. Wang, Q. Wang, M. Tan, et al., J. Alloys Compd. 922 (2022) 166260.
[35] X. Zhang, D. Chen, Y. Zhou, et al., Chin. Chem. Lett. 32 (2021) 1161–1164.
[36] C. Wang, R. Yu, W. Luo, et al., Nano Res. 15 (2022) 9019–9025.
[37] C. Chi, Z. Liu, G. Wang, et al., Adv. Energy Mater. 13 (2023) 2302055.
[38] X. Han, T. Chen, P. Zhang, et al., Adv. Funct. Mater. 32 (2021) 2109672.
[39] W. Xu, H. Li, X. Zhang, et al., Adv. Funct. Mater. 34 (2024) 2309509.
[40] B. Sun, Q. Zhang, W. Xu, et al., Carbon 201 (2023) 776–784.
[41] X. Ma, N. Xiao, J. Xiao, et al., Carbon 179 (2021) 33–41.
[42] Y. Sun, H. Wang, W. Wei, et al., ACS Nano 15 (2021) 1652–1665.
[43] R. Jiao, Z. Deng, L. Lei, Y. Liu, J. Cui, J Energy Storage 74 (2023) 109486.
[44] M. Tang, S. Zhu, Z. Liu, et al., Chem 4 (2018) 2600–2614.
[45] J. Yang, Y. Zhai, X. Zhang, et al., Adv. Energy Mater. 11 (2021) 2100856.
[46] X. Chen, J. Tian, P. Li, et al., Adv. Energy Mater. 12 (2022) 2200886.
[47] H. Liu, H. Du, W. Zhao, et al., Energy Storage Mater. 40 (2021) 490–498.
[48] Y. Huang, X. Zhong, X. Hu, et al., Adv. Funct. Mater. 34 (2024) 2308392.
[49] S. Wu, H. Peng, L. Huang, et al., Inorg. Chem. Front. 10 (2023) 5908–5916.
[50] M. Gu, L. Fan, J. Zhou, A.M. Rao, B. Lu, ACS Nano 15 (2021) 9167–9175.
[51] B. Li, J. Zhao, Z. Zhang, et al., Adv. Funct. Mater. 29 (2018) 1807137.
[52] W. Zhou, B. He, L. Quan, et al., Adv. Energy Mater. 13 (2022) 2202874.
[53] L. Yan, Q. Ren, J. Wang, et al., ACS Appl. Mater. Interfaces 14 (2022) 48715–48726.
[54] H.J. Kim, N. Voronina, H. Yashiro, S.T. Myung, ACS Appl. Mater. Interfaces 12 (2020) 42723–42733.
[55] T. Hosaka, K. Kubota, H. Kojima, S. Komaba, Chem. Commun. 54 (2018) 8387–8390.
[56] M.F. Zhou, P.X. Bai, X. Ji, et al., Adv. Mater. 33 (2021) e2003741.
[57] C. Zhang, Y. Xu, M. Zhou, et al., Adv. Funct. Mater. 27 (2017) 1604307.